Materials & Design 222 (2022) 111026

Contents lists available at ScienceDirect

Materials & Design

journal homepage: www.elsevier.com/locate/matdes

Precipitation, mechanical properties and early slant ductile fracture in cyclic and naturally aged Al-Zn-Mg(-Cu) alloys

Sohail Shah [a,*], Akash Gopal [a], Elisabeth Thronsen [b], Constantinos Hatzoglou [a], Bjørn Holmedal [a]

[a] Department of Materials Science and Engineering, Norwegian University of Science and Technology (NTNU), 7491 Trondheim, Norway
[b] Department of Physics, Norwegian University of Science and Technology (NTNU), N-7491 Trondheim, Norway

HIGHLIGHTS

- The implications of cyclic ageing on strength, ductility and more importantly fracture has been investigated.
- Early shear/slant fractures are reported to occur for cyclic and naturally aged plate alloys.
- Plate materials with an underaged microstructure are more prone to such slant fracture as compared to axisymmetric materials.

GRAPHICAL ABSTRACT

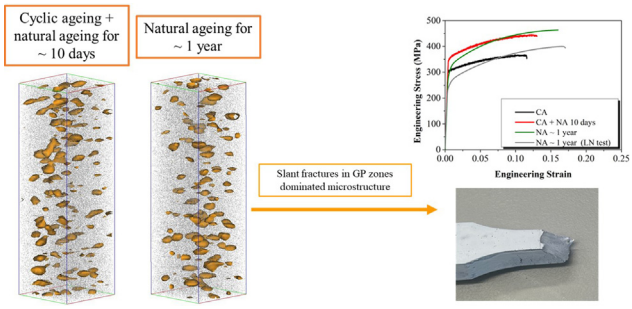

ARTICLE INFO

Article history:
Received 14 June 2022
Revised 25 July 2022
Accepted 2 August 2022
Available online 5 August 2022

Keywords:
Aluminum alloys
Atom probe tomography (APT)
Slant fractures
Cyclic ageing
Natural ageing

ABSTRACT

Natural and artificial ageing treatments are compared with ageing by cyclic deformation at room temperature. Atom probe tomography and transmission electron microscopy revealed that a fine distribution of GP-zones, was responsible for the strength after cyclic ageing. Ten days further natural ageing allowed these early-stage clusters to grow into more stable ones, thereby improving the mechanical response. This resulted in similar tensile strength and uniform elongation as for the peak aged condition by artificial ageing. It was found that fracture of cyclic aged samples occurred earlier, in the form of a ductile slant shear fracture without necking in advance. In all cases, the slant fracture started at about the same point as reaching maximum strength, i.e., at the uniform limit. However, by an artificial ageing treatment after the cyclic hardening treatment, an ordinary necking behavior was seen, similar as for the peak aged samples. Natural aged samples had similar GP-zones as the cyclic hardened ones, and the same slant fracture mode, indicating that the precipitation structure controls the fracture type. Similar behavior was observed for two different Al-Zn-Mg alloys, with and without copper.

1. Introduction

Aluminum alloys aged by precipitation hardening have a good combination of strength, formability, corrosion resistance and low weight, making them attractive as engineering materials. The alloying elements in supersaturated solid solution after solution heat treatment and quenching, forms a high number of nano-sized precipitates that act as obstacles for dislocation movement and thereby strengthen the alloy. In Al-Zn-Mg alloys, similar high strength can be obtained either by natural ageing (NA) for several months or by artificial ageing (AA) for some hours [1].

After quenching, the density of vacancies is also supersaturated. The vacancies play an important role for the precipitation. They are required to facilitate substitutional diffusion of the solute atoms and play a role for the cluster nucleation. In general, diffusion,

* Corresponding author.
E-mail address: sohail.shah@ntnu.no (S. Shah).

https://doi.org/10.1016/j.matdes.2022.111026
0264-1275/

and hence precipitation kinetics, are faster at elevated temperatures, as the equilibrium concentration of vacancies and their diffusivity increases with temperature [2]. However, the driving force for nucleation increases with higher supersaturation at lower temperatures [3]. The optimal combination of temperature and time for the conventional precipitation ageing, is always a compromise between these two factors.

Recently, Sun *et al.* [2] demonstrated that aluminum alloys can be processed at room temperatures with cyclic plasticity, providing strength and uniform elongation equivalent or slightly exceeding the peak aged (PA) condition. The repetitive cyclic deformation leads to dragging of jogs on dislocations, which produces vacancies [4] and thereby facilitates local diffusion at room temperature.

With precipitation and deformation occurring simultaneously, the process becomes more complex. The plastic straining will influence the precipitation. In general, nucleation and growth are accelerated as a result of the local vacancy generation by glide of heavily jogged dislocations during plastic deformation [5,6]. As argued by Sun *et al.* [2] the repeated shearing of the clusters might prevent their early growth and enable an increased number of nuclei to form. The dislocations may act as heterogeneous nucleation sites for precipitates, which was reported by Deschamps *et al.* [7] for cases of artificial ageing of a pre-strained Al-Zn-Mg alloy. Dynamic strain ageing occurs in Al-Zn-Mg alloys, causing heterogenous plastic deformation and involving local substitutional pipe diffusion of Zn and Mg around temporarily stored dislocations [8–10].

Hutchinson *et al.* [11] studied the room temperature cyclic deformation behavior of underaged and peak aged Al-Zn-Mg-Cu alloys for different plastic strain amplitudes, strain rates and number of cycles. Based on small angle X-ray scattering measurements, they concluded that the nucleation rate of GP zones formed during cyclic deformation remained constant. Based on their characterization, they vaguely suggested that the size of the GP zones did not increase significantly during the cyclic treatment, suggesting continuous nucleation and restricted growth of the GP-zones during cyclic deformation.

Even though it takes months of storage at room temperature, NA can in some cases be an interesting alternative for achieving the desired strength for Al-Zn-Mg alloys. Also, NA plays an important role for the welding properties [12]. Interestingly, higher work hardening, higher uniform elongation and higher uniform strength, as well as a yield strength similar to the artificially peak aged condition, was reported to be obtained by NA of an Al-Zn4.8-Mg1.4 alloy [13]. However, in some cases, an early shear fracture has been reported to occur, rather than ordinary necking in tensile tests of naturally aged alloys [14–16]. Chung et al. [15] found for an as quenched 7075 alloy, that the shear fracture was replaced by ordinary necking instability at low temperature tests and suggested that the reason for shear fractures may be the dynamic strain ageing phenomenon, associated with the Portevin-Le Chatelier effect in this type of alloys [17]. The early fracture may make the NA alloy less suited for applications in energy absorbing safety parts, e.g., in automotive applications.

The specific purpose of this study is to investigate the effect of systematic cyclic ageing (CA) at different frequencies on strengthening of two Al-Zn-Mg(-Cu). Most of the investigations are done on the 7046 alloy, however some experiments on a copper [18] free leaner 7003 alloy have also been done. The mechanical properties and work hardening imparted to the alloy as a result of the CA, are studied by tensile testing. Atom probe tomography has been employed to characterize the clusters formed after the CA. Special emphasis has been given to the type of fracture causing these samples to fail, which is characterized by light optical and scanning electron microscopy.

2. Experimental

A commercial 7046 and 7003 alloy with composition Al-6.5Zn-1.3 Mg-0.3Cu-(Fe,Zr,Si) and Al-5.7Zn-0.7 Mg-0.01Cu-(Fe,Zr,Si) respectively measured by spectrograph analysis, was received from Benteler automotive as extruded 6 mm thick plates. The thermomechanical treatment performed in this study involves 40 min of solution heat treatment (SHT) at 480 °C in a salt bath followed by a drop quench in cold water. This is done to retain a complete solid solution. Then the samples are strengthened by either NA, AA or CA treatments.

Samples with the tensile axis along the extrusion direction were machined with dimensions suited for CA tests. They had a square cross section of 6x6 mm^2 and a short uniform length of 12 mm, to avoid buckling during the compression part of the cyclic loading. Detailed information about the sample geometry can be found in the supplementary information. Selected samples were grounded and polished for micro hardness testing, using a 1000 gf Vickers indenter with 5 parallel readings for each condition.

The cyclic loading experiments were designed based on the study in reference [11] and [2]. During each cycle, the engineering stress σ was varied sinusoidally through tension and compression by a prescribed stress amplitude σ_a. The stress amplitude was increased systematically from cycle to cycle. At cycle number n, it was prescribed as

$$\sigma_n = \sigma_0 + (\sigma_t - \sigma_0)\sqrt{\frac{n}{N}} \tag{1}$$

Here σ_0 is approximately the initial yield stress of the material (after solution heat treatment), σ_t is the targeted strength (close to the initial yield stress of the conventional PA sample), and N is the total number of cycles, applied to reach the desired stress. Hence, the CA tests were stress controlled, using an INSTRON 250KN with a servo-hydraulic test system. All tests were carried out at room temperature.

Strain measurements during the cyclic experiments were carried out using a digital image correlation [19] system developed by Fagerholt [20]. It consists of a high-speed CCD camera with a resolution of 1280 × 1024 pixels capturing digital images at a rate ranging from 1 to 50 frames per second. The rate was varied according to the frequency of the cycle sampled in each test. The samples were sprayed with a white background on the gauge area, followed by decoration with a black speckle pattern. The speckles are used by the DIC software to track the strain during deformation. This method of calculating strain is accurate and provides strain field maps to check for any strain localization.

A virtual extensometer for the tensile test was obtained from the DIC processing, by tracking the length change between two selected points at the specimen surface, having an initial distance $l_0 = 12mm$. All plots are based on the nominal tensile stress and the nominal strain calculated by this virtual extensometer.

The sinusoidal load cycle n consists of first a maximum nominal tensile stress σ^n_{max}, then a minimum nominal compression stress σ^n_{min}. Each cycle contributes to two stress ranges: $\Delta\sigma^{2n-1}$ from the maximum to the minimum stress, and $\Delta\sigma^{2n}$ from the minimum to the maximum stress of the next cycle.

$$\Delta\sigma^{2n-1} = \sigma^n_{max} - \sigma^n_{min}, \Delta\sigma^{2n} = \sigma^{n+1}_{max} - \sigma^n_{min} \tag{2}$$

The corresponding nominal strain ranges Δe^{2n-1} and Δe^{2n} are calculated as

$$\Delta e^{2n-1} = e^n_{max} - e^n_{min}, \Delta e^{2n} = e^{n+1}_{max} - e^n_{min} \tag{3}$$

The corresponding plastic part of the strain ranges Δe^{2n-1}_p and Δe^{2n}_p were computed as

$$\Delta e_p^{2n-1} = \Delta e^{2n-1} - \frac{\Delta\sigma^{2n-1}}{E}, \Delta e_p^{2n} = \Delta e^{2n} - \frac{\Delta\sigma^{2n}}{E} \quad (4)$$

where E is the elastic modulus. The first onloading Δe_p^1 requires special treatment

$$\Delta e_p^1 = e_{max}^n - \frac{\sigma_{max}^1}{E} \quad (5)$$

The cumulative plastic strain is defined as e_{cp}^i at each extrema, as

$$e_{cp}^i = \sum_{k=1}^{i} \Delta e_p^k \quad (6)$$

Hence, for each cycle n, the cumulative plastic strain is recorded at the maximum and minimum points, at $i = 2n-1$ and $i = 2n$, respectively.

The grain structure was investigated using an optical microscope. The sample surface was first grinded on progressively finer grades of SiC paper up to 4000 mesh and then the surface was polished using 3 μm and 1 μm diamond paste. Finally, the samples were chemically polished using active oxide suspension (OP-U) to obtain a smooth and scratch free surface. The grain structure was revealed by anodizing the polished samples using 5% fluoroboric acid (HBF4) for 45 s at an applied voltage of around 12 V at ambient temperature. The samples were examined in an optical microscope with polarized light. The distribution of the intermetallic particles and the fracture surface were studied using the scanning electron microscopy (SEM).

Atom Probe Tomography (APT) samples were prepared using the FEI Helios Focused Ion Beam (FIB) using Ga^+ as the ion source. Electropolishing was attempted as it was the preferred methodology, though the CA samples fractured. Silicon microtip coupons provided by Cameca Inc. were used to deposit the lamella and sharpened to around 100 nm to produce the APT needles. The specimens were sharpened by using a 16 kV Ga^+ beam followed by a 2 KV final cleanup step to remove higher concentrations of implanted high-energy Ga ions. The APT sample with NA for 1 year was prepared following a two-step standard electropolishing process [21], since unlike the CA samples, had high yield in the preferred electropolishing method.

All APT analyses were carried out using a Local Electrode Atom Probe (LEAP) 5000XS by Cameca Instruments Inc. This is a straight flight path instrument with a detection efficiency of 80%. All samples were run at 25 K base temperature in laser mode with a detection rate of 0.5%. Depending on the sample geometry, it was calibrated in the range of 70–100 pJ. A pulse rate of 250 kHz was used for all the samples. Datasets, ranging from 50 to 150 million ions, were collected from the samples. The reconstructions and the post processing analyses were carried out using the Integrated Visualization and Analysis Software (IVAS) by Cameca Instruments Inc and the Norwegian Atom Probe App [22]. The latter has been developed in Norwegian University of Science and Technology (NTNU) by C. Hatzoglou and is an open access software dedicated to APT data treatment [23]. The estimation of the reconstruction parameters was carried out using the structural information, according to the protocols of Gault et al. [24]. The size of clusters is defined based on the $Extent_z$ parameter as explained in [25] and the number densities are measured by taking the ratio of the number of clusters identified to the number of atoms in the dataset. This is done by also taking into account detection efficiency of the APT and the average atomic volume. The uncertainty is calculated by dividing the number density by the square root of the total number of clusters.

The TEM samples were prepared by first grinding down bulk samples to ~100 μm and punching out to 3 mm disks. The specimens were subsequently electropolished in a Struers TenuPol-5 machine using an electrolyte mixture consisting of 1/3 HNO_3 and 2/3 CH_3OH. The applied voltage was 20 V and the liquid was kept at −25 ± 5 °C. An image and probe corrected JEOL JEM-ARM200CF microscope operated at 200 kV was used to collect the high-angle annular dark-field scanning TEM (HAADF-STEM) images. The convergence semi-angle was 27 mrad, while the inner-and outer semi-angles were 67 and 155 mrad, respectively. The high-frequency noise in the images was reduced using an inverse fast Fourier transform (FFT) filtering by applying a low-pass mask on the FFT of approximately 6.7 nm^{-1} and then taking the inverse FFT of the masked FFT. The selected area diffraction patterns (SADP) and bright-field (BF) images were acquired on a JEOL 2100 microscope operated at 200 kV.

3. Results

CA of 7046 alloy was carried out at different frequencies to examine the plastic strain accumulation within the samples during the tension–compression cycles. Times ranging from 5 sec/cycle to 120 sec/cycle were used for 420 cycles.

3.1. CA and hardness

The stress amplitude (σ_0) for the first cycle was very close to the yield stress of the material in the solutionized state (~120 MPa) and the targeted strength (σ_{max}) was 370 MPa. Higher strengths (σ_{max}) were tested but resulted in fracture during the CA. To limit the amount of damage being inflicted onto the sample, the final strength was chosen slightly lower than the yield strength of the PA sample. The optimization of σ_{max} is shown in detail in the supplementary information. After this initial optimization study, a combination of 420 cycles and σ_{max} = 370 MPa were chosen.

To check the stability of the strength of the samples immediately after their CA treatment, hardness tests were carried out afterwards on the samples that had been cyclically aged at 7.5, 40 and 120 sec/cycle, respectively. As shown in Fig. 1, the hardness increases sharply during the first few hours after the cyclic ageing and then gradually less until around 10 days. After around 10 days, the hardness from the CA region has saturated.

The strain was measured by DIC during each cyclic ageing test. The plastic strain range Δe_p was calculated at two points per cycle

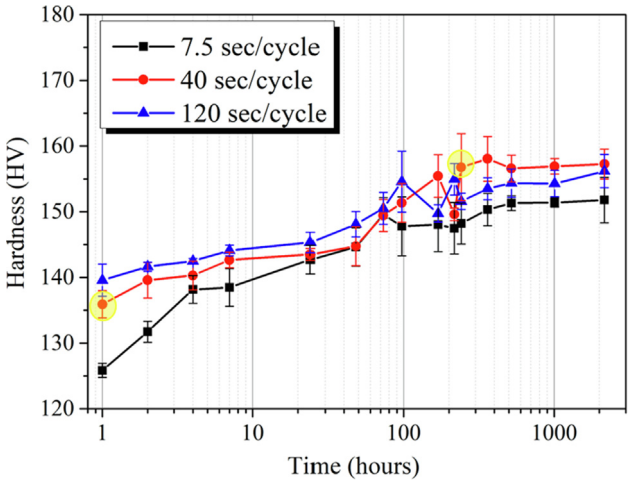

Fig. 1. Hardness measurements for 7046 alloy at room temperature as a function of time after quenching. The different time/cycle from the CA used here are: 7.5 sec/cycle, 40 sec/cycle, and 120 sec/cycle. The yellow circles indicate the conditions selected for the microstructural analyses. (For interpretation of the references to colour in this figure legend, the reader is referred to the web version of this article.)

according to Equation (4). As can be seen from Fig. 2, the highest frequencies lead to the largest amount of plastic strain in each cycle. The fastest, 5 sec/cycle sample fractured before completing the 420 cycles. This is evident from Fig. 2a, where the plastic strain increases rapidly, before ending in a fracture. From Fig. 2, the 60 and 120 sec/cycle tests with the lowest frequencies and the longest time spent for each cycle, went through the least amount of plastic strain range during each cycle.

In Fig. 3, the square of the stress amplitude increases linearly with the cumulative plastic strain, similar as earlier reported by Hutchinson et al. [11]. However, for the 5 and 7.5 sec/cycle conditions, the curve is no longer linear at cumulative strains larger than around 2.

Optimizing the frequency for better mechanical response is a trade-off between imposing the sufficient amount of plastic deformation that is required for the cyclic hardening to occur and limiting the plastic strain to avoid too much damage during the plastic deformation, potentially leading to fracture. The 40 sec/cycle sample gave the best mechanical response, as seen from Fig. 2d.

3.2. Mechanical testing of the 7046 alloy

Tensile tests were carried out immediately after the CA experiments and after 10 days of further storage at room temperature. To confirm any statistical fluctuations within the strength measurements, 5 tests were performed for each of the optimized conditions. Tensile tests for the PA condition and for a specimen with NA for one year are also included in Fig. 3. for comparison. The yield stress was larger for the PA condition than for any other condition, while the NA alloy had the largest uniform strain but the lowest YS as seen in Table 1.

The tensile tests of 7046 alloy done immediately after the cyclic treatment did not reach the initial yield stress (YS) of the PA sample but showed about the same uniform elongation (408 vs 596 MPa and 9.6% vs 10%). Nor the samples treated by CA + NA 10 days of reached the YS of the PA condition (447 vs 496 MPa). However, as can be seen from Fig. 3a and Table 1, all cyclic aged samples with 10 days of subsequent storage consistently surpassed the UTS of the PA sample, with a 12% increase in the UTS from 475 MPa ± 12 MPa to 532 MPa ± 10 MPa, as compared to without the 10 days of storage. The maximum strength reached after 10 days is similar for all frequencies tested and similar to the one-year NA condition. The average yield strength increased from 408 MPa ± 8 MPa to 446 MPa ± 2.9 MPa after 10 days of storage, a 9.4% increase in YS

For both 7003 and 7046 alloy, the PA sample had a significant amount of necking before fracture occurred, while the cyclic aged samples fractured before reaching the maximum load. The fracture, as observed from the transverse plate direction, consisted of a 45° plane fracture surface without any visual signs of necking. To investigate if the shear fracture was due to damage evolution during the cyclic loading, the CA samples were afterwards artificially aged at 140 °C for 8 h and then tensile tested. Interestingly, the PA condition and CA + AA 140 °C sample had similar strengths and similar normal necking behavior, as seen by the fracture strengths from Fig. 3b for 7046 alloy and Fig. 4b for 7003 alloy.

The cumulative plastic strain evolution of the 7046 alloy is shown in Fig. 3c for all cases, as calculated from Equation (6). Almost all the curves are nearly straight lines, except for the samples run at lowest time per cycle (5 and 7.5 sec/cycle), for which fracture occurred during the CA. The true fracture strains measured by inspecting the projected area of the fracture surface for all conditions, is listed in the supplementary information.

3.3. Mechanical testing of 7003 alloy

To rule out any role played by Cu in causing the early shear fractures, similar tensile CA processing and corresponding tensile tests as for the 7046 alloy, were performed on a Cu free 7003 alloy. The resulting tensile tests are shown in Fig. 4a for the samples fractured in slant mode without pronounced necking. An identical trend is seen as compared to the 7046 alloy, where the CA and CA + 10 days sample undergo the same type of early shear fractures near the point where the stress reaches the UTS, while the PA and CA + PA and a NA 1 year sample was Peak aged, all underwent necking behavior prior to fracture as seen in Fig. 4b. For this alloy the CA + 10 days specimens reached a similar YS as the PA samples,

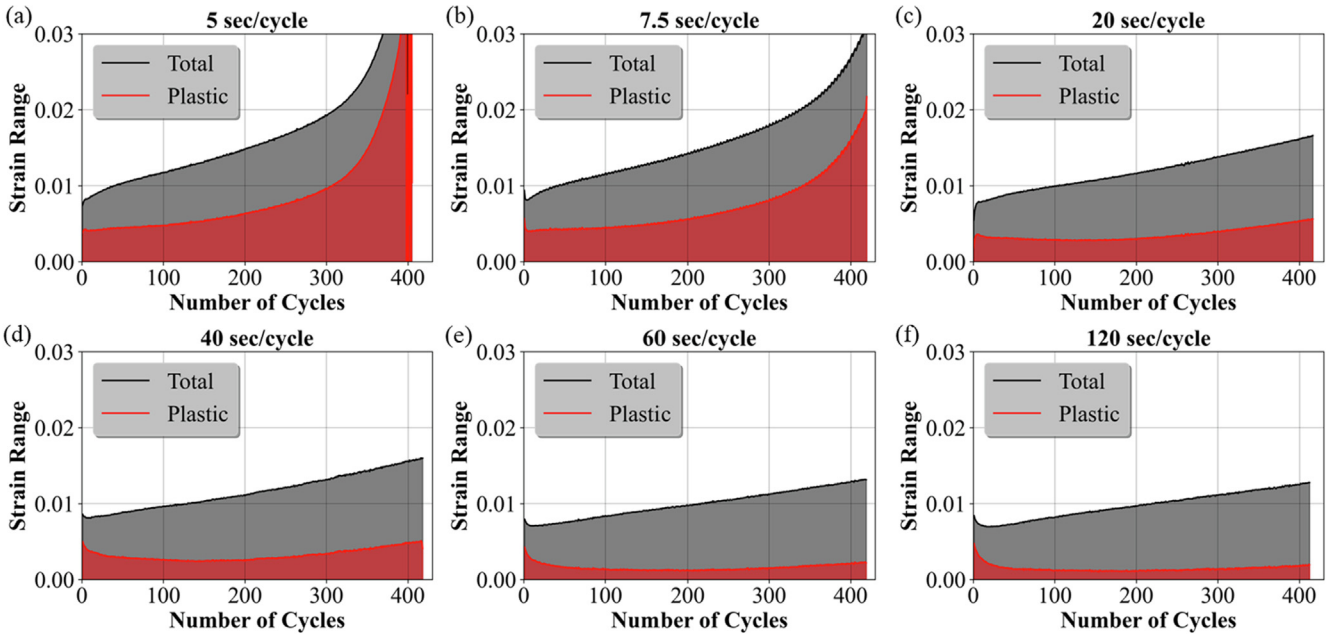

Fig. 2. Measured total strain range Δe and plastic strain range Δe_p during CA experiments of 7046 alloy at time/cycle ranging from (a) 5 sec/cycle - (f) 120 sec/cycle, as indicated.

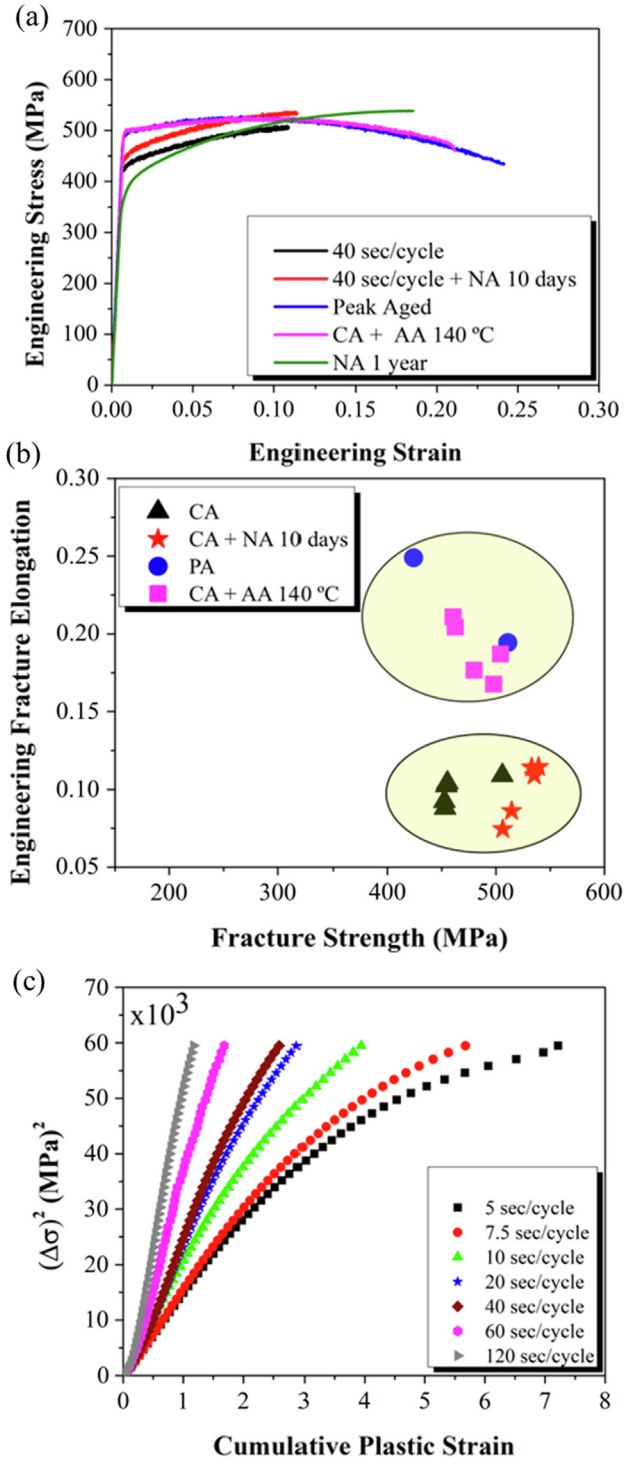

Fig. 3. (a) Mechanical response of the 7046 alloy with stress–strain plots showing a comparison of CA, NA, PA and CA + AA. Fracture strengths for the corresponding stress strain plots are summarized in (b). (c) the square of the stress amplitude is plotted as a function of the cumulative plastic strain, for all tests, ranging from 5 sec/cycle to 120 sec/cycle. The nominal strain rate of the tensile tests was $1.4.10^{-3}$.

while the NA for one year reached both a larger UTS and a larger uniform strain than any of the others.

3.4. TEM and APT of the 7046 alloy

To help understand the origin of the strength gained by CA, APT and HRTEM were used to characterize the microstructure. Detailed quantitative microstructural analysis can be found in Ref [25]. Some additional HAADF-STEM images and SADPs from the 7046 alloy in the CA, CA + 10 days and NA 1 year are provided in Appendix B. Consistently with the work in Ref. [25], these additional images provide evidence that the same type of clusters and GP zones are present in the three conditions, mainly GPI zones and smaller clusters. Microstructural investigations with BF-TEM revealed dislocations that are present both in CA and CA + NA 10 days condition, as seen in Fig. 5(a and b).

In addition, the NA 1 year condition has been investigated by APT to compare the chemistry of the GP zone evolution. As seen from Table 2,which is based on cluster identification, the concentrations of Zn and Mg in the clusters do not change from CA to 10 days of storage after CA, while the size increases but is still smaller than after 1 year of NA. Furthermore, the number density increased during the 10 days of storage after CA. NA for 1 year showed that the number density is consistently lower than the CA condition.

3.5. Fracture surfaces

The fracture surfaces, after failure of the cyclic aged samples, were inspected using a scanning electron microscope (SEM). From a macroscopic level, the fracture appears to be in a shear mode making an approximately 45° angle to the transverse axis of the plate specimen. This was the case for all cyclically aged samples of 7046 and 7003 alloy (supplementary information) that were tested in uniaxial tension until fracture. A high number of dimples were seen, with particles inside many of them. Energy dispersive spectroscopy (EDS) of these particles, as shown in Fig. 6 for 7046 alloy, revealed mainly iron rich particles. Some regions had a high density of dimples, but also flat regions without dimples were present, as seen in Fig. 6(b).

Optical micrographs, taken from the transverse direction, reveal non-recrystallized grains that are elongated in the extrusion direction, as shown in Fig. 7(b) for the case of 7046 alloy (7003 supplementary information). An overview of the fracture mode in shear is provided in Fig. 7(a). On a finer scale in Fig. 7, near the fracture surface, it can be seen from the bending of the grain boundaries close to the fracture surface, that most of the grains did undergo shear deformation near the fracture surface just before fracture occurred, indicating a ductile fracture mode. There is a presence also of grains that abruptly end without visible deformation, indicating some cases of grain boundary fracture, though not the dominating mode.

4. Discussion

4.1. Parameter optimizations for CA of 7046 alloy

Optimization of the CA treatment involved 3 main parameters: frequency, target stress and the number of cycles. Higher frequencies led to a large amount of cumulated plastic strain. The back and forward glide of jog-dragging dislocations is assumed to generate vacancies locally, but when the frequency of the load is high, there seems not to be enough time for the vacancies that are generated to contribute to the clustering. With lower frequencies, the measured amount of cumulative plastic strain was reduced, offering the time needed for the local solute diffusion that is required to form clusters. The minimum amount of plastic strain accumulation was obtained with the lowest frequencies (0.016 Hz, 0.008 Hz). These gave very similar strength as the 0.025 Hz sample, which therefore was chosen as the optimum condition to minimize the time spent during the cyclic ageing.

Table 1
Measured tensile properties under different test conditions for 7046.82. All measurements are based on the standard deviation of 5 values.

	Yield Strength (MPa)	UTS (MPa)	Fracture Strength (MPa)	Elongation at Uniform Strain (%)	Elongation at fracture (%)
CA	408 ± 8	475 ± 17	464 ± 23	9.6 ± 1	10 ± 0.9
CA + NA 10 days	447 ± 3	532 ± 10	526 ± 14	9.6 ± 1.8	10 ± 1.8
NA 1 year	364	535	531	18.3	18.3
Peak Aged	496	530	467	10	22
CA + AA 140 °C	503 ± 6	532 ± 9	481 ± 20	9.4 ± 0.7	18 ± 3.3

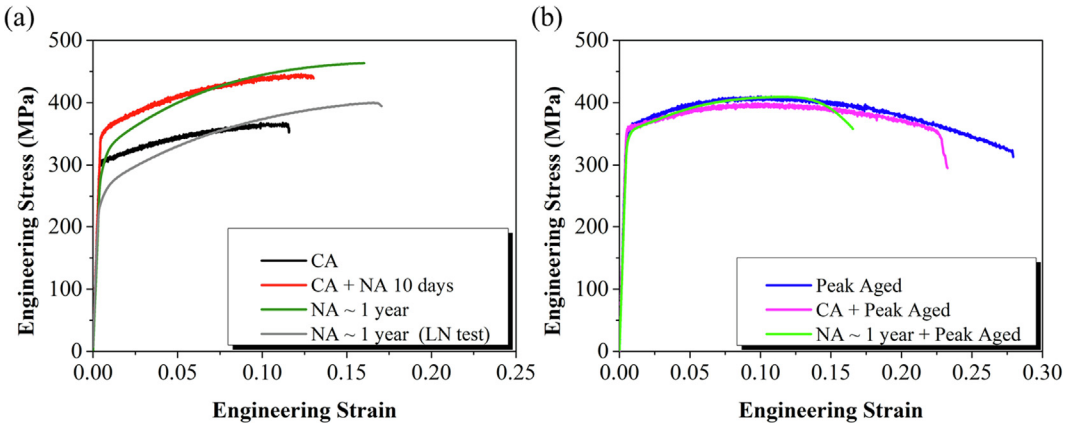

Fig. 4. Tensile stress–strain curves of the 7003 alloy for all samples that had (a) slant fractures and (b) fracture in the neck. The strain rate of the tensile tests was $1.4.10^{-3}$. LN is liquid nitrogen test (−196 °C).

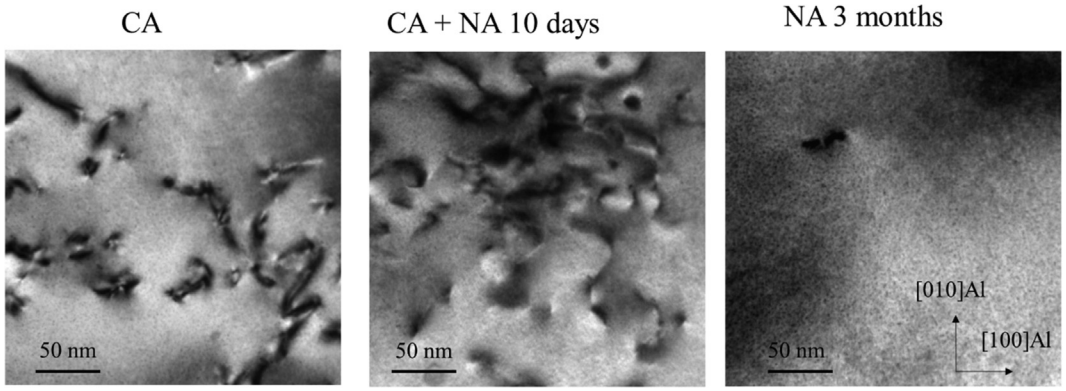

Fig. 5. BF-TEM images of 7046 (a) CA, (b) CA + NA 10 days and (c) NA 1 year conditions showing the presence of dislocations in the cyclically aged conditions.

Table 2
Cluster analysis data for APT datasets shown in Fig. 5.

Condition	Composition (At%)	Number Density ($10^{24}/m^3$)	Size (nm)	Zn/Mg Ratio
CA	Mg- 7.43 ± 1.45 Zn- 12.17 ± 1.69 Cu- 0.39 ± 0.21	1.81 ± 0.18	1.12 ± 0.52	1.64 ± 0.71
CA + NA 10 days	Mg- 8.03 ± 0.66 Zn- 12.58 ± 1.21 Cu- 0.24 ± 0.11	3.15 ± 0.23	1.50 ± 0.89	1.58 ± 0.48
NA 1 year	Mg- 7.98 ± 0.33 Zn- 11.55 ± 0.48 Cu- 0.29 ± 0.07	2.29 ± 0.61	1.85 ± 0.88	1.46 ± 0.17

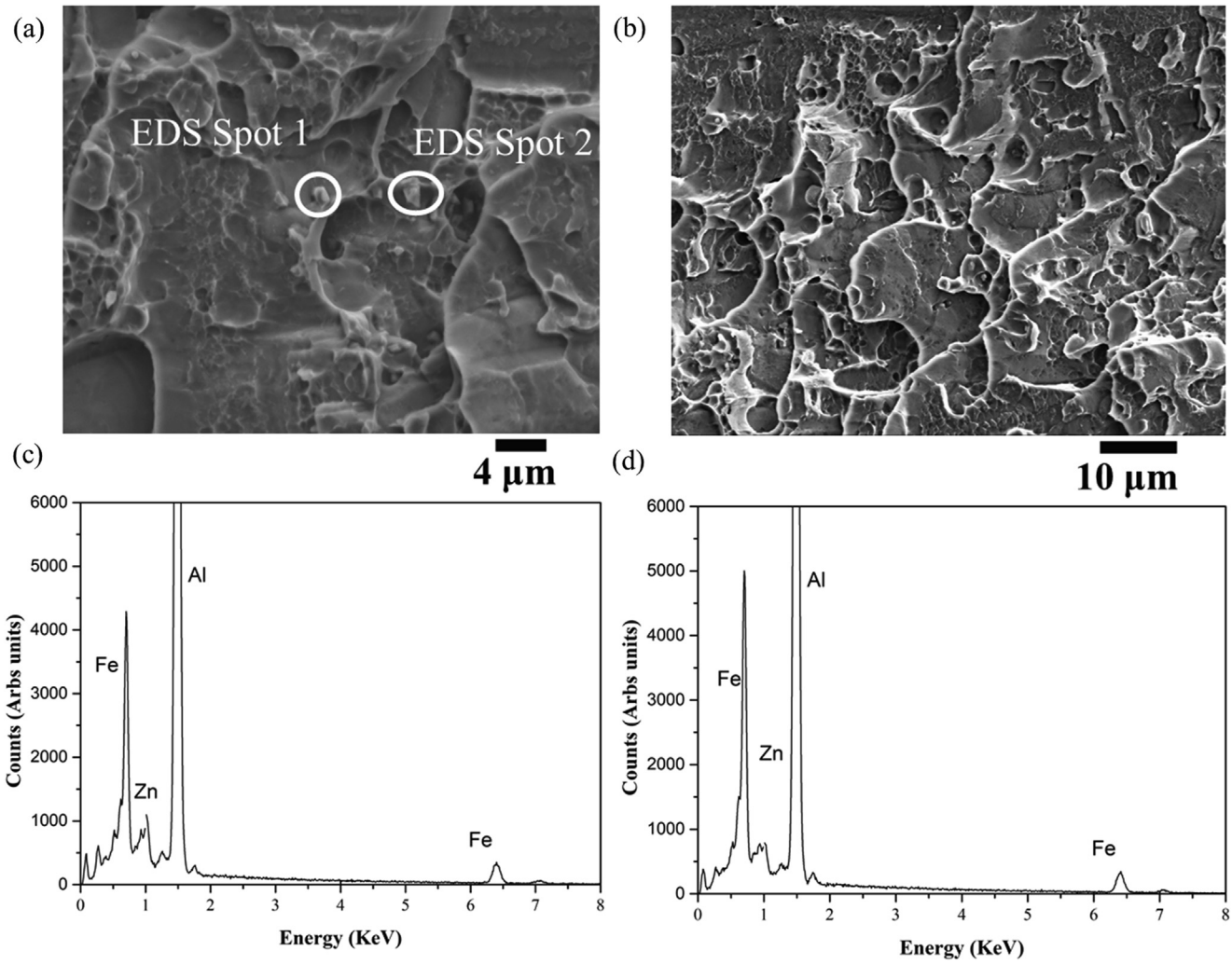

Fig. 6. (a) SEM micrograph of the dimples seen on the fracture surface of the 40sec/cycle sample for 7046 alloy. (b-d) showing the EDS spectra of the iron rich intermetallic particles.

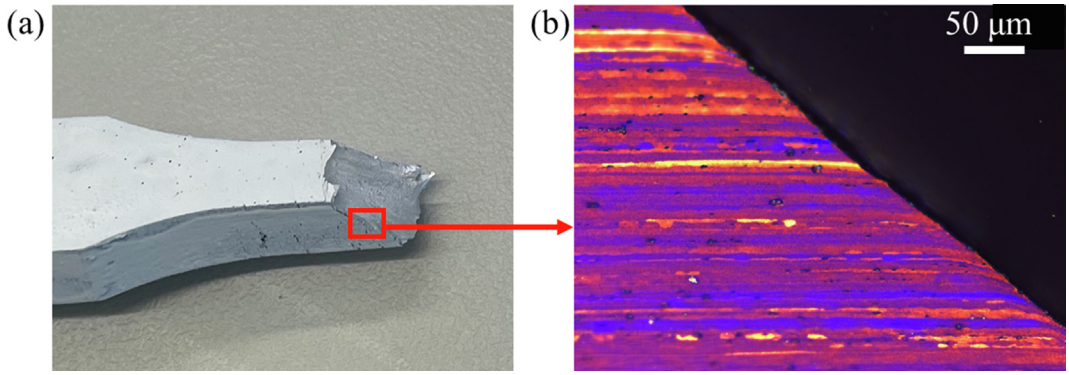

Fig. 7. (a) Optical micrograph of the shear fracture location after a uniaxial tensile test of 7046 alloy. (b) Higher magnification optical micrograph of the grains ending at the shear fracture, taken from the transverse direction.

4.2. Microstructure and mechanical response of 7046 alloy

From the series of mechanical tests done after CA and 10 days of storage (NA), higher strengths are reached, while maintaining similar elongations, within the statistical measuring variation, which is in good agreement with what was reported by Sun *et al.* [2]. The cyclic plasticity forms dislocations as well as excess vacancies [26]. This speeds up the kinetics of supersaturated elements in the matrix, forming a high number density of solute clusters [2] (of the order of $10^{24} m^{-3}$), which are seen in atom probe immediately after the CA. The increase in strength is attributed to the clusters, which are found to be extremely fine and uniformly distributed after the CA.

Based on extensive SAXS and APT investigations, Hutchinson et al. [11] concluded that the back and forward gliding dislocations during the CA repetitive shears the clusters and thereby keeps their size small and maintain their nucleation rate. However, there are still excess vacancies present after finishing the cyclic loading, which for a while enable faster local diffusion of elements in substitutional solid solution during the subsequent storage and enhance further growth of the small clusters present after the cyclic ageing. The increased size of the clusters makes them more difficult to cut by gliding dislocations and hardens the material. As a result, the hardness increases most rapidly during the first few hours of storage after the cyclic ageing treatment. In other words, the clusters immediately after CA grow further during storage. However, after 10 days of NA after the CA, the further strength increase is very slow.

From the APT and TEM analysis of the alloy after 10 days of storage, a combination of larger clusters along with smaller ones similar to those seen immediately after CA, are observed. This may indicate that either cluster nucleation is still occurring, resulting in new small clusters, or there is a coarsening of the clusters, where the smaller ones are subcritical in size and dissolving. This indicates that the cluster structure is still evolving, but the measured hardness is not changing much anymore. The NA 1 year condition revealed a very similar microstructure to the CA + NA 10 days condition with a slightly decreased Zn/Mg ratio indicating the coarsening of the microstructure to developed GP zones. The average size of clusters has slightly increased as compared to the CA + NA 10 days condition c.f. Table 2 and Fig. 8d and e. Similar strengths for the NA 1 year as compared to the CA + NA 10 days can be strongly related to the similar microstructure in the two conditions.

Size estimates from APT data by a cluster identification method are expected to be sensitive to the considered representative material volume, and since the considered clusters are fine, a precise cluster analysis is challenging [27]. Hence, to provide an additional qualitative judgment of the trend on the evolution of the precipitate sizes, as seen by the cluster identification method, we also show the pair correlation function (PCF) in Appendix A. Analyzing the radial distribution function, as described by Zhao *et al.* [28] and also implemented in the previous study for the same alloy [25] provides a statistical approach, which gives a somehow better estimation of the average values within a dataset. Consistent with the cluster identification method, it can be concluded, also from analyzing the PCFs, that the size increased during the 10 days of storage after CA and the size after NA for 1 year is consistently larger than for the CA conditions.

Although the accumulated plastic strain during CA is large, most of the generated dislocations during the tensile load are removed during the reversal compression part of the cycle. A qualitative comparison between the dislocations observed by BF-TEM in Fig. 5, and dislocations seen by BF-TEM in the 2% pre-strained alloys seen in the work of Stemper *et al.* [18], suggests that fewer dislocations are seen in CA conditions than by this relatively small pre-strain. The strength contribution from the dislocations stored during CA is smaller than the monotonic pre-strain contribution of about 60 MPa, as estimated by Stemper *et al.*[18]. Since the strength, as well as the structure and chemistry of the GP zones, are quite similar for the CA and NA conditions, it is reasonable that the strength contribution from the GP zones is dominant, and that the contribution from the dislocations present in the CA conditions is very small compared to this.

4.3. Slant fractures in CA and NA samples

Surprisingly, the CA, CA + NA 10 days, and also the NA conditions, all experienced slant, ductile shear fractures for both 7046 and 7003 alloys. This fracture mode occurred at about the same strain as the uniform strain predicted by the Considère criterion for the onset of diffuse necking. The UTS and the uniform elongation reached after 1 year of NA were higher than for the CA samples, indicating stronger work hardening for the NA condition and that the shear fracture seems to occur at the maximum force. The effect of Cu does not seem to influence the fracture mode since very similar results were obtained for the Cu free 7003 alloy.

Pedersen et al. [29] demonstrated similar abrupt shear fractures instead of diffuse necking, in tensile tests of a 7075 T651 alloy. In their investigation, the fracture was mainly brittle and following the grain boundaries. Whereas in the alloys studied here, the fracture can be regarded as mainly ductile, due to the presence of dimples and the bending of the grains close to the fracture surface as seen in Fig. 7b. Only a few grains do not undergo bending/deformation.

Fe containing intermetallic constitutive particles are known to nucleate damage during plastic deformation, and thereby contribute to a decreased ductility [30]. Their size and number density increases with the Fe content. Such particles were observed in the bottom of the dimples in the fracture surfaces. The damage and void nucleation seem to be correlated with these particles. The question is whether the damage occurred as part of a flow instability leading to the shear fracture, or if the damage accumulated due to the plastic cyclic deformation, i.e., low-cycle fatigue, was the reason for the fracture to occur? To shed light on this question, the cyclically aged tensile samples for both 7046 and 7003 alloys, with accumulated low-cycle fatigue damage, were artificially aged at 140 °C for ~ 8 h. As this resulted in diffuse necking, similar to the peak aged condition and with considerable ductility (see Figure Fig. 3d and Fig. 4b), it is reasonable to argue that the shear fracture is not caused by the damage accumulated during the cyclic plastic deformation.

The microstructure after the subsequent artificial ageing is assumingly dominated by η' precipitates [31], as opposed to the high number density of clusters in the CA microstructure. Since the η' precipitates are well developed and larger precipitates, there will be more solute left in the matrix in the CA condition than it is after the subsequent artificial ageing. The Zn and Mg content of atoms in solid solution in the matrix will contribute to dynamic strain ageing (DSA). The Portevin Le Chatelier (PLC) instability, causing serrated yielding, can be seen as a few MPa serrations on the stress strain curves. The DSA can modify and enhance the strain localization during fracture. Chung *et al.* [15] observed a similar type of slant shear fracture, but for an as quenched 7075 alloy with significantly stronger dynamic strain ageing due to higher amounts of Mg and Zn in solid solution in this condition. Since they observed normal diffuse necking for tensile tests performed at −196 °C, where the strain rate sensitivity was found to be positive, i.e. no DSA, they concluded, that the reason for this fracture mode in their case was the DSA. The fact that this type of shear fracture for 7003 alloy was found in both NA and cyclic aged conditions at room temperature as well as at −196 °C (LN test), suggests that DSA is not the sole reason to the slant fractures observed for the NA and CA conditions considered here.

Wang *et al.* [32] observed similar shear fractures in C-Mn steels at elevated temperatures, at which dynamic strain ageing occurs in these alloys. They observed similar fracture surfaces, which are commonly referred to as slant fractures for these alloys. They found from finite element simulations that PLC bands, either inclined or conical PLC bands, traversed the uniform region during testing of thick tensile specimens. The conical bands lead to cup and cone fracture, while the inclined bands lead to ductile shear fractures, similar to those reported here. Note that simulations of an isotropic C-Mn steel [33] showed that the choice between a slant fracture and an axisymmetric cup and cone fracture depends

sensitively on symmetry breaking perturbations. Hence, for a plate material with an orthotropic anisotropy, the slant fracture might be preferred. Furthermore, this might explain why the shear fracture did not occur in tensile tests of the axisymmetric Al-Zn-Mg cyclic aged alloy tested by Sun *et al.* [2]. Finite element models containing different cracks in Al 2024 T3 alloys observed the direction of maximum effective plastic strain at the onset of crack growth to be strongly correlated with the orientation of the slant fracture surface[34].

Fig. 4a and b distinguish the conditions that underwent slant fractures and diffuse necking phenomenon respectively. A clear trend is seen wherein the conditions with a microstructure of early-stage clusters and GP zones (as seen from the atom probe results in Fig. 8) undergo slant fractures while the microstructure, which is more developed and dominated by η', undergoes diffuse necking. While the influence of DSA has been ruled out with the tests carried out at −196 °C (LN tests, see Fig. 4), the possible reason for these early slant fractures seem to be a combination of microstructure and plate material with an orthotropic anisotropy.

This type of fracture has not been reported for the cyclic aged Al-Zn-Mg alloys in earlier investigations [2]. It involves a very local shear flow instability. This fracture mode can be important in applications involving plastic deformations, e.g. in energy absorbing structures used for safety constructions like bumpers and crash boxes in a car. Precautions should be taken considering applications of cyclic and/or NA Al-Zn-Mg alloys in such safety constructions, where plastic deformations are involved. An interesting question is, whether this fracture mode may play a role also after artificial ageing, say for underaged conditions?

5. Conclusions

Processing parameters for room temperature cyclic aging have been optimized with respect to strength and ductility for two Al-Zn-Mg(-Cu) alloys. APT and TEM characterization after cyclic ageing reveal a high number density of clusters that grow during the subsequent NA occurring during 10 days of storage at room temperature and contributes to increased strength, while maintaining about the same uniform elongation in tensile tests.

An early shear fracture, denoted a slant fracture, is reported to occur for cyclic and for NA Al-Zn-Mg(-Cu) plate materials. Fracture surface investigations revealed dimples and plastically deformed grains near the fracture surface, from which it is concluded that it is a plastic flow instability causing the ductile shear fracture. Due to the presence of a normal diffuse necking instability after subsequent artificial ageing, it is concluded that the imposed fatigue damage during the cyclic deformation is not causing this instability and fracture mode. Furthermore, the same fracture mode is reported for the two alloys with and without Cu. The potential role of dynamic strain ageing in these early slant fractures was ruled out by low temperature tests in liquid nitrogen. It is argued that plate materials might be more prone for this fracture mode than axisymmetric materials. Special attention is required when considering cyclic or NA of Al-Zn-Mg alloys for applications requiring ductility at high strengths.

6. Data availability

The raw data used to reproduce the presented results are available in the Zenodo repository https://doi.org/10.5281/zenodo.6342915

CRediT authorship contribution statement

Sohail Shah: Conceptualization, Investigation, APT, DIC and Mechanical testing data curation, Writing- original draft, Visualisation. **Akash Gopal**: Investigation, DIC and Mechanical testing data curation. **Elisabeth Thronsen**: Investigation, TEM data curation. **Constantinos Hatzoglou**: Supervision, Writing- review and editing. **Bjørn Holmedal**: Conceptualisation, Investigation, Supervision, Writing- review and editing.

Declaration of Competing Interest

The authors declare the following financial interests/personal relationships which may be considered as potential competing interests: Sohail Shah reports financial support was provided by Norwegian University of Science and Technology. Sohail Shah reports a relationship with Norwegian University of Science and Technology that includes: employment. N/A.

Acknowledgement

The authors wish to thank Hanne-Sofie Søreide for her support in the APT lab. The Research Council of Norway (RCN) is acknowledged for funding the NTNU atom probe facility through the Norwegian Laboratory for Mineral and Materials Characterization (MiMaC) project number: 269842. The RCN is further acknowledged for the support to the Norwegian Micro-and Nano-Fabrication Facility, NorFab. We thank Benteler automotives for providing material to carry out the study. The (S)TEM work was conducted on the NORTEM (NFR: 197405) infrastructure at the TEM Gemini Centre, Trondheim, Norway. E.T. acknowledges the NTNU Digital Transformation initiative 'Alldesign' and the 'SumAl' (NFR: 294933) project, supported by Hydro, Benteler Automotive Raufoss AS and Neuman Aluminium.

Appendix A. APT analysis

The *iso*-position method (IPM) [35] was used to identify clusters. This methodology is based on a solute concentration criterion, where a concentration value is estimated for each atom in the analyzed volume. A concentration threshold of $C_{threshold}$ = 14% was used, for which the concentration histogram of a randomized dataset is negligible (less than 0.1%). A minimum number of atoms, N_{min} = 36 or 40 was required for the cyclic and cyclic +10 days condition, to ensure that no clusters were identified in a randomized volume with $C_{threshold}$. A detailed explanation of how the clusters are defined and identified can be found elsewhere [35,36]. A sub volume from each dataset was extracted and visualized to have a closer look at the clusters shown through Fig. 8(a) and (b), showing that 10 days further storage of the sample after the CA resulted in slightly larger clusters compared to the ones found immediately after CA.

The PCFs are plotted for Zn and Mg in Fig. 8 (d and e). As explained by De Geuser and Gault [27], an increase in the width of the PCF indicates an increased correlation length, i.e. an increased cluster size. Hence, the PCFs suggests that the cluster size increased during the 10 days of storage after CA, and that the cluster sizes are larger for the NA for 1 year condition than for the CA condition.

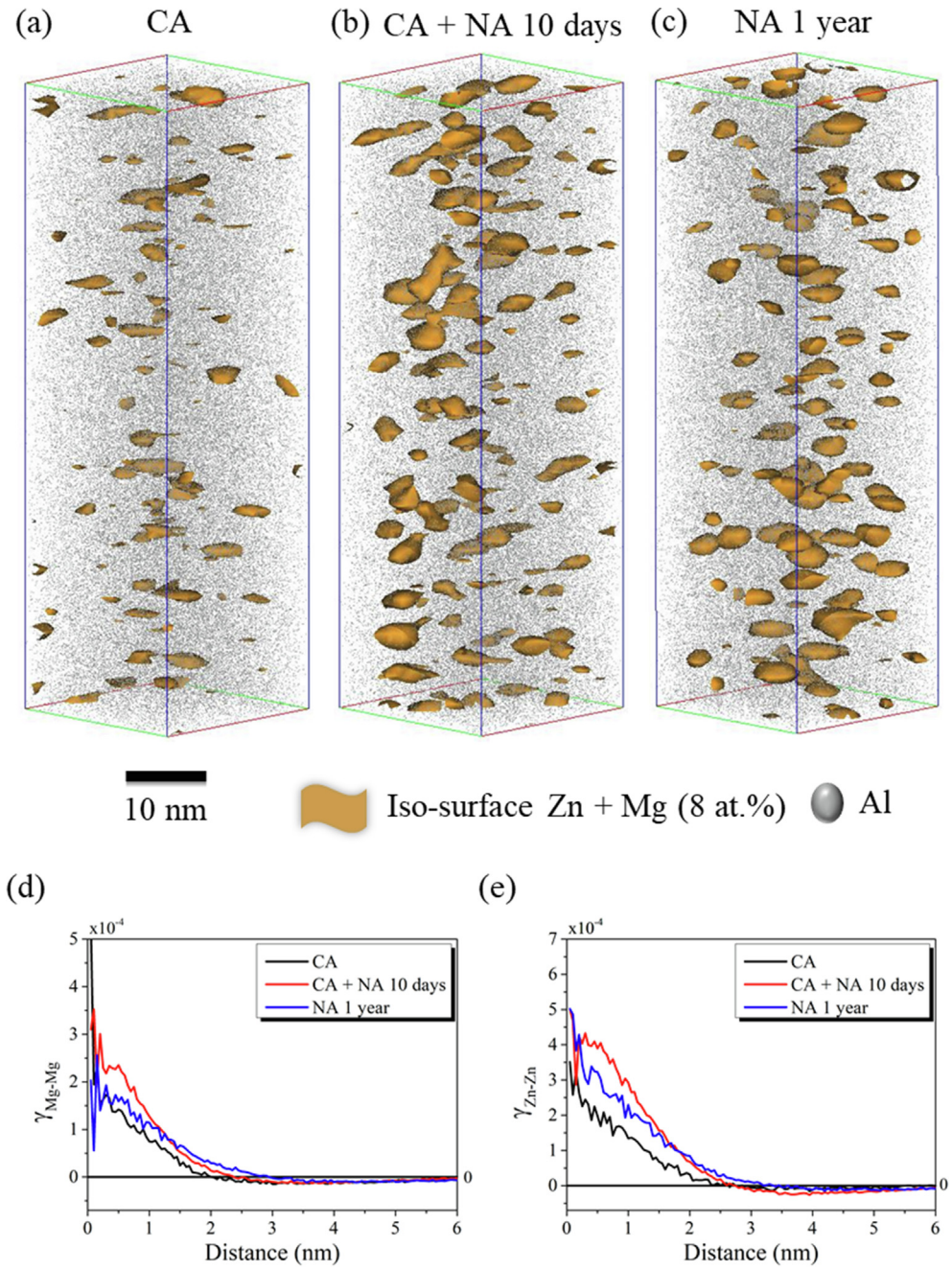

Fig. 8. 25 × 25 × 80 nm^3 region of interest chosen from the 7046 APT datasets to magnify the visualization of clusters in the respective condition in (a) CA, (b) CA + NA 10 days and (c) NA 1 year. PCF of the above shown APT datasets for (d) Mg-Mg and (e) Zn-Zn pairs.

Appendix B. HAADF-STEM

Fig. 9 shows HAADF-STEM images in (a), (c), (e) and SADP in (b), (d) and (f) from the 7046 alloy in the CA, CA + 10 days and NA 3 months condition. The 3 months condition was chosen here since it is very similar in terms of hardness with the NA 1 year condition. The blue disks in the SADPs indicate the diffracted intensities from the clusters and exhibit good correspondence with the ones presented in Refs.. Both the HAADF-STEM images and SADP provide evidence that the same type of clusters, mainly GPI zones, are present in all three conditions.

Appendix C. Supplementary Information

Supplementary data to this article can be found online at https://doi.org/10.1016/j.matdes.2022.111026.

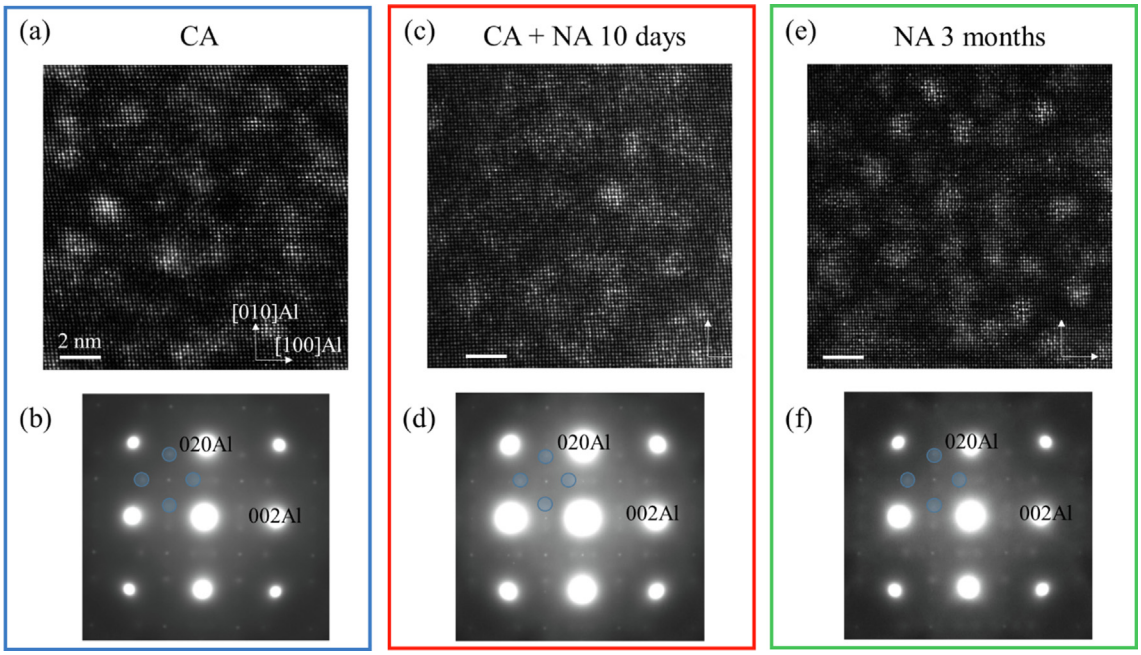

Fig. 9. (a), (c), (e): HAADF-STEM images of the clusters in the CA, CA + 10 days and NA 3 months for 7046, respectively. (b), (d), (f): SADP from CA, CA + 10 days and NA 3 months for 7046, respectively. The blue disks in the SADPS indicate the diffracted intensities from the clusters, showing that the same type of clusters prevail in all three conditions. (For interpretation of the references to colour in this figure legend, the reader is referred to the web version of this article.)

References

[1] E. Hornbogen, Hundred years of precipitation hardening, J. Light Met. 1 (2) (2001) 127–132.
[2] W. Sun, Y. Zhu, R. Marceau, L. Wang, Q.i. Zhang, X. Gao, C. Hutchinson, Precipitation strengthening of aluminum alloys by room-temperature cyclic plasticity, Science 363 (6430) (2019) 972–975.
[3] D.A. Porter, K.E. Easterling, Phase transformations in metals and alloys (revised reprint), CRC press, 2009.
[4] G. Saada, Production de défauts ponctuels par écrouissage dans un métal cubique à faces centrées, Physica 27 (7) (1961) 657–660.
[5] H.D. Chandler, J.V. Bee, Cyclic strain induced precipitation in a solution treated aluminium alloy, Acta Metall. 35 (10) (1987) 2503–2510.
[6] W.Z. Han, Y. Chen, A. Vinogradov, C.R. Hutchinson, Dynamic precipitation during cyclic deformation of an underaged Al–Cu alloy, Mater. Sci. Eng., A 528 (24) (2011) 7410–7416.
[7] A. Deschamps, F. Livet, Y. Bréchet, Influence of predeformation on ageing in an Al–Zn–Mg alloy—I. Microstructure evolution and mechanical properties, Acta Mater. 47 (1) (1998) 281–292.
[8] M. Hörnqvist, B. Karlsson, Effect of heat treatment on the strain hardening behaviour of an Al–Zn–Mg alloy, Int. J. Mater. Res. 100 (11) (2009) 1574–1581.
[9] E. Pink, W.M. Webernig, Precipitation during serrated flow in AlZn5Mg1, Acta Metall. 35 (1) (1987) 127–132.
[10] P.u. Zhou, Y. Song, L. Hua, J. Lu, J. Zhang, F. Wang, Mechanical behavior and deformation mechanism of 7075 aluminum alloy under solution induced dynamic strain aging, Mater. Sci. Eng., A 759 (2019) 498–505.
[11] C.R. Hutchinson, F. de Geuser, Y. Chen, A. Deschamps, Quantitative measurements of dynamic precipitation during fatigue of an Al–Zn–Mg–(Cu) alloy using small-angle X-ray scattering, Acta Mater. 74 (2014) 96–109.
[12] I. Kalemba, M. Kopyściański, C. Hamilton, S. Dymek, Natural Aging Behavior of Friction Stir Welded Al-Zn-Mg-Cu Aluminum Alloys, Arch. Metall. Mater. 60 (2) (2015) 875–879.
[13] P. Zhang et al., Solute cluster evolution during deformation and high strain hardening capability in naturally aged Al–Zn–Mg alloy, Acta Mater. 207 (2021) 116682.
[14] J. Chen, Y. Madi, T.F. Morgeneyer, J. Besson, Plastic flow and ductile rupture of a 2198 Al–Cu–Li aluminum alloy, Comput. Mater. Sci. 50 (4) (2011) 1365–1371.
[15] N. Chung, J.D. Embury, J.D. Evensen, R.G. Hoagland, C.M. Sargent, Unstable shear failure in a 7075 aluminum alloy, Acta Metall. 25 (4) (1977) 377–381.
[16] A. Fjeldly, H.J. Roven, Effects of strain rate and anisotropy on the tensile deformation properties of extruded AlZnMg alloys, Metall. Mater. Trans. A 31 (3) (2000) 669–678.
[17] E. Pink, W. Bernt, M. Fellner, Flow and fracture of aluminum alloys and of iron and steel within and outside the range of inhomogeneous flow, Scripta Metallurgica et Materialia; (United States) 28 (9) (1993).
[18] L. Stemper et al., Giant hardening response in AlMgZn (Cu) alloys, Acta Mater. 206 (2021) 116617.
[19] L.T. Stephenson, M.P. Moody, P.V. Liddicoat, S.P. Ringer, New techniques for the analysis of fine-scaled clustering phenomena within atom probe tomography (APT) data, Microsc. Microanal. 13 (6) (2007) 448–463.
[20] E. Fagerholt, Field measurements in mechanical testing using close-range photogrammetry and digital image analysis, 2012.
[21] B. Gault, et al., Atom probe microscopy. Vol. 160. 2012: Springer Science & Business Media.
[22] S. Samudrala, O. Wodo, S.K. Suram, S. Broderick, K. Rajan, B. Ganapathysubramanian, A graph-theoretic approach for characterization of precipitates from atom probe tomography data, Comput. Mater. Sci. 77 (2013) 335–342.
[23] Atom Probe Tomography (APT) - Department of Materials Science and Engineering - NTNU. 2022; Available from: https://www.ntnu.edu/ima/research/apt.
[24] B. Gault, M.P. Moody, F. de Geuser, G. Tsafnat, A. La Fontaine, L.T. Stephenson, D. Haley, S.P. Ringer, Advances in the calibration of atom probe tomographic reconstruction, J. Appl. Phys. 105 (3) (2009) 034913, https://doi.org/10.1063/1.3068197.
[25] S. Shah, E. Thronsen, C. Hatzoglou, S. Wenner, C.D. Marioara, R. Holmestad, B. Holmedal, Effect of cyclic ageing on the early-stage clustering in Al–Zn–Mg (-Cu) alloys, Mater. Sci. Eng., A 846 (2022) 143280, https://doi.org/10.1016/j.msea.2022.143280.
[26] L. Shi et al., The effect of chemical patterning induced by cyclic plasticity on the formation of precipitates during aging of an Al–Mg–Si alloy, Mater. Sci. Eng., A 815 (2021) 141265.
[27] F. De Geuser, B. Gault, Metrology of small particles and solute clusters by atom probe tomography, Acta Mater. 188 (2020) 406–415.
[28] H. Zhao, B. Gault, D. Ponge, D. Raabe, F. De Geuser, Parameter free quantitative analysis of atom probe data by correlation functions: Application to the precipitation in Al-Zn-Mg-Cu, Scr. Mater. 154 (2018) 106–110.
[29] K.O. Pedersen, T. Børvik, O.S. Hopperstad, Fracture mechanisms of aluminium alloy AA7075-T651 under various loading conditions, Mater. Des. 32 (1) (2011) 97–107.
[30] J.A. Taylor, The effect of iron in Al-Si casting alloys. in 35th Australian foundry institute national conference, Australian Foundry Institute (AFI), 2004.
[31] H. Löffler, I. Kovács, J. Lendvai, Decomposition processes in Al-Zn-Mg alloys, J. Mater. Sci. 18 (8) (1983) 2215–2240.
[32] H. Wang, C. Berdin, M. Mazière, S. Forest, C. Prioul, A. Parrot, P. Le-Delliou, Portevin–Le Chatelier (PLC) instabilities and slant fracture in C-Mn steel round tensile specimens, Scr. Mater. 64 (5) (2011) 430–433.
[33] S. Ren, M. Mazière, S. Forest, T.F. Morgeneyer, G. Rousselier, A constitutive model accounting for strain ageing effects on work-hardening. Application to a C-Mn steel, Comptes Rendus Mécanique 345 (12) (2017) 908–921.
[34] W. Lan, X. Deng, M.A. Sutton, C.-S. Cheng, Study of slant fracture in ductile materials, Int. J. Fract. 141 (3-4) (2006) 469–496.
[35] W. Lefebvre, F. Vurpillot, X. Sauvage, Atom probe tomography: put theory into practice, Academic Press, 2016.
[36] J.M. Hyde, G. DaCosta, C. Hatzoglou, H. Weekes, B. Radiguet, P.D. Styman, F. Vurpillot, C. Pareige, A. Etienne, G. Bonny, N. Castin, L. Malerba, P. Pareige, Analysis of radiation damage in light water reactors: comparison of cluster analysis methods for the analysis of atom probe data, Microsc. Microanal. 23 (2) (2017) 366–375.